DOI: 10.21062/mft.2025.061 http://www.journalmt.com

Push-Type Rotary Steering Mandrel Mechanical Analysis and Life Prediction

Wenzhe Li (0009-0009-3547-4074)[1], Ye Chen (0009-0004-2665-2231)[1*], Jichuan Zhang (0009-0008-7947-460X)[2,3], Xudong Wang (0009-0009-2242-369X)[1], Pengcheng Wu (0009-0007-8542-920X)[1], Chengyu Ma (0009-0009-9133-8122)[4], Xiumei Wan (0009-0000-5556-9403)[1], Xing Chen (0009-0005-1747-6763)[2,3]
[1]Engineering Technology Research Institute, PetroChina Southwest Oil &Gasfield Company, Chengdu, Sichuan, 610017, China
[2]CNPC Chuanqing Drilling Engineering Company limited, Chengdu, Sichuan, 610055, China
[3]Top of Energy technology Company, Chengdu, Sichuan, 610032, China
[4]PetroChina Southwest Oil &Gasfield Company, Chengdu, Sichuan, 610055, China
[*]Email: chensmile0318@163.com

The push-type rotary steerable core bearing has high load capacity and high precision, and has been widely used in oil and gas drilling field. Its service life is difficult to predict due to various complex working conditions. Based on the finite element method, this paper establishes a three-dimensional rotating guide mandrel model to calculate and analyze the mechanical simulation of the guide mandrel under different working conditions, and establishes the corresponding life prediction model to predict its life. The results show that reducing the torque and speed in the range of drilling requirements is conducive to improving the overall life of the spindle, and the life matrix and life distribution are consistent with the characteristics of S-N curve, which is consistent with the characteristics of high cyclic stress of the spindle. The research results can be used to reliably predict the life of the push-type rotary steering mandrel and simulate its working state with high precision. This data is critical for reliability analysis and design optimization.

Keywords: Rotary steerable system, Finite element method, Life prediction, S-N fatigue.

1 Introduction

Oil and gas resources are important resources, and drilling is the core of exploration and development of oil and gas resources. China is now seeking out unconventional oil and gas resources, such as shale, low permeability, ultra-deep water, and deep water, in addition to conventional oil and gas resources. Rotary steerable drilling technology is representative and advanced in the field of oil and gas drilling, and it is widely used in offshore and onshore oil fields in China [1]. According to the different guidance methods, rotary steerable drilling system can be divided into two types: push-pull rotary guidance means that the force applied to the wall near the drill bit makes it react on the drill tool near the drilling point, so as to achieve the purpose of guidance; Directional turning guidance is to apply a certain directional force to the drill mandrel in the hole, and use the centralizer to act on the fulcrum near the bit to deflect the drill inclination [2].

Scholars at home and abroad have carried out a lot of research on rotary steerable drilling tools.

In 2019, based on the BHA bending beam method, Li et al. [3] built a mechanical model of the push-back type gyro guide drilling tool with variable section, established the inclination calculation model, and studied the law of the influence of structural parameters, bit weight, bit anisotropy, drillability and other factors on the inclination performance of the drilling tool. In 2021, Bi et al. [4] studied the influence of factors such as borehole curvature, borehole inclination, steering force and bit weight on RSBHA statics performance of static push-up rotary steering drilling tools, taking two-dimensional oriented Wells as the research object. In 2022 Zeng et al. [5] established a mechanical analysis model of push-back RSBHA based on the finite element method and the theory of transverse and horizontal curved beams. Taking the main components of push-back rotary steerable system as an example, the influences of bit pressure, stabilizer and flexible short-section parameters on the force and deformation of push-back RSBHA were analyzed. In 2023, Jia et al. [6] established a mechanical analysis model of 475 static push-type rotary steering-tool assembly (RSBHA) based on the theory of vertical and horizontal curved beams. By simulating and analyzing the overall distribution of RSBHA bending stress, the influencing factors of maximum bending stress and the variation rules of RSBHA, the fatigue failure risk of the system in the high-formation slope well section was prevented. In 2024, He et al. [7] used Lagrange equation to build a dynamic model of a full-well drill pipe system, discretized it by finite element method, and carried out numerical simulation by Newmark-

beta method to study the effects of centralizer placement, flexible joint size, weight on bit and other factors on the dynamic characteristics and safety of rotary steering tools. It is found that domestic and foreign scholars mainly focus on the mechanical analysis of rotary steerable drill assembly, but lack the mechanical analysis of the push-type rotary steerable shaft and the prediction of its service life.

As the most complex bearing component in the steering actuator, the rotary steering mandrel has multiple cross section changes inside and outside the pipe, and a number of hydraulic channels and connecting holes are set up in the pipe wall. Secondly, it is in the complex working environment at the bottom of the hole, bearing the torque transmitted by the upper drilling tool and the weight on bit transmitted by the bottom bit. Therefore, this paper takes the rotary guide mandrel as the research object, and conducts finite element simulation analysis of the rotary guide mandrel under different load conditions through Abaqus software to study the mechanical analysis of the push-type rotary guide mandrel under different working conditions, so as to ensure its strength requirements during work and further analyze the life of the mandrel.

2 Modeling and meshing of rotating mandrel

2.1 Mechanical analysis model of rotary guide mandrel

Based on the finite element theory, the guide shaft is regarded as a bar structure, and the guide shaft is divided into n smaller elastic elements, the end points of which are nodes. Since the guide shaft is divided into tiny elements with length l, the mass and stiffness of each element can be concentrated on the nodes. The finite element discrete model of the guide shaft is shown in Fig. 1. Interpolation also expresses the displacement of each point in the element on the node. We accurately analyze each unit's characteristic parameters before solving them. The mass matrix and stiffness matrix of the discrete model of the whole structure of the guiding shaft are obtained by superimposing the characteristic parameters of each node by the method of set [8].

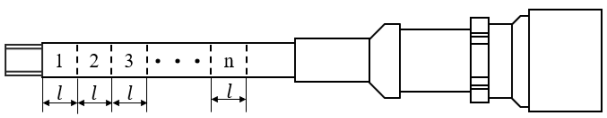

Fig. 1 *Guide mandrel finite element discrete model diagram*

For any unit of the discrete model, take the displacement of the unit node $u_i(t)$ and $u_{i+1}(t)$ write the calculation formula of the displacement as the node coordinate column:

$$u(x,t)=\sum_{i=1}^{2}N_i(x)u_i(t) \tag{1}$$

Where:

$N_i(x)$ …The shape function of the unit, representing the unit displacement of one node coordinate, and the static deformation function of the unit when the coordinates of the remaining nodes are zero.

The shape function of the unit is:

$$N_1(x)=1-x/l\ ,N_2(x)=x/l \tag{2}$$

Substitute the element form function into equation (1) to form the continuous displacement field inside the element. The matrix form is [9]:

$$\mathbf{u}(x,t)=\begin{bmatrix}1-\frac{x}{l} & \frac{x}{l}\end{bmatrix}^{\mathrm{T}}\begin{bmatrix}u_1(t) & u_2(t)\end{bmatrix}^{\mathrm{T}} \tag{3}$$

According to equation (3), the kinetic energy and potential energy of the unit are calculated as follows:

$$\mathbf{T}_e=\frac{1}{2}\int_0^l\rho S\left[\frac{\partial u(x,t)}{\partial t}\right]^2\mathrm{d}x=\frac{1}{2}\dot{\mathbf{u}}_e^{\mathrm{T}}\mathbf{m}_e\dot{\mathbf{u}}_e \tag{4}$$

$$\mathbf{V}_e=\frac{1}{2}\int_0^l ES\left[\frac{\partial u(x,t)}{\partial x}\right]^2\mathrm{d}x=\frac{1}{2}\mathbf{u}_e^{\mathrm{T}}\mathbf{k}_e\mathbf{u}_e \tag{5}$$

Where:

ρ …The cell density;

E …The elastic modulus of the element;

s …The cross section area;

$\mathbf{u}_e$ …The element displacement matrix;

$\mathbf{m}_e$ …Half yen mass matrix;

$\mathbf{k}_e$ …The element stiffness matrix;

$\dot{\mathbf{u}}_e$ …The unit velocity matrix;

e …Any unit in the discrete model.

Assuming that the guiding axis is a linear material, the ρS and $E S$ is constant, and the mass matrix and stiffness matrix of the element can be obtained from equations (3) and (4) as follows:

$$\mathbf{m}_e=\frac{\rho Sl}{6}\begin{bmatrix}2 & 1\\ 1 & 2\end{bmatrix},\mathbf{k}_e=\frac{ES}{l}\begin{bmatrix}1 & -1\\ -1 & 1\end{bmatrix} \tag{6}$$

There is an axial load on the guiding axis, and a distributed axial force acts on the element, then the generalized force of the element is [10]:

$$F_e=\int_0^l f(x,t)N\mathrm{d}x \tag{7}$$

According to the relationship between node coordinates and global coordinates, the mass matrix $\mathbf{m}_e$, stiffness matrix $\mathbf{k}_e$ and generalized force of element F_e are combined into mass matrix $\mathbf{M}$, stiffness matrix $\mathbf{K}$ and generalized force of system $\mathbf{F}$ structure by group set method.

$$\mathbf{M} = \frac{\rho S l}{6}\begin{bmatrix} 8 & 2 & 0 \\ 2 & 6 & 1 \\ 0 & 1 & 2 \end{bmatrix} \tag{8}$$

$$\mathbf{K} = \frac{ES}{l}\begin{bmatrix} 4 & -2 & 1 \\ -2 & 3 & -1 \\ 0 & -1 & 1 \end{bmatrix} \tag{9}$$

$$\mathbf{F} = \begin{bmatrix} F_{e1}^{\mathrm{T}} & F_{e2}^{\mathrm{T}} & F_{e3}^{\mathrm{T}} \end{bmatrix}^{\mathrm{T}} \tag{10}$$

Where:

M …The mass matrix;

K …The stiffness matrix;

F …The generalized force of system.

According to the Lagrange equation, the dynamic equation of the discrete model of the guiding axis structure in the global coordinate system is as follows:

$$\mathbf{M}\ddot{x} + \mathbf{K}x = \mathbf{F}(t) \tag{11}$$

2.2 Simulation

Using SolidWorks 3D modeling software, 3D solid modeling is carried out according to the actual size measured on site [11], as shown in Fig. 2. The geometric model of the total assembly mainly includes the rotating mandrel, the upper and lower plain bearings, the lower joint, and other parts, and the total length of the model is 1727 mm. The material of the rotating spindle is 15-15HS MAX, the elastic modulus is 191000 MPa, and Poisson's ratio is 0.3. The density is kg/m³ and the yield strength is 965MPa.

Secondly, the established three-dimensional model of the rotating mandrel is imported into Hypermesh software for grid rendering. To obtain a mesh with the same specifications, set the regular cylindrical surface on the rotating mandrel structure as a mapping surface mesh. The mesh is drawn separately on irregular geometric surfaces such as grooves, and the inner and outer meshes of the bearing contact surface are drawn as common nodes to ensure the accuracy of calculation. The result of grid division is shown in Fig. 3.

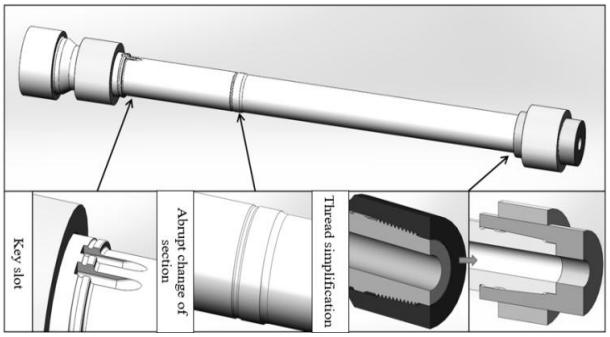

Fig. 2 *Rotating mandrel geometry model diagram*

Fig. 3 *Grid division result diagram*

The total number of nodes is 400,782 and the total number of units is 537,759. It includes 329,375 C3D8R linear hexahedral elements, 200,906 C3D4 linear tetrahedral elements, and 7478 C3D5 linear pyramid elements.

In order to investigate the influence of different load parameters on the mechanical properties of the mandrel of the push-type rotary steerable tool, the external load applied to the model can be changed step by step according to the actual drilling process to solve the calculation.

When the strength of mechanical parts is checked for safety, the "maximum stress method at dangerous section" and "safety factor method at dangerous section" are often used. The maximum stress at the dangerous section is obtained by finite element simulation, and the strength meets the requirements by comparing the mechanical parameters of the selected materials with the safety factor selected in the design of drilling tools. Common drill design experience parameters are shown in Tab. 1.

Tab. 1 *Empirical parameter of safety factor*

σs/σb	0.45~0.55	0.55~0.70	0.70~0.90	casting
S	1.2~1.5	1.4~1.8	1.7~2.2	1.6~2.5

3 Finite element simulation

3.1 Drilling condition analysis

First of all, the routine working conditions of normal drilling are calculated, and a variety of loads applied on the rotating mandrel are set with reference to the actual working conditions on site. The maximum working conditions of drilling pressure is 140kN, torque is 19kN·m, and pushing force is 20kN are taken. Abaqus software carried out static calculation and simulation of the model, and the force cloud diagram of the rotating mandrel under the maximum normal drilling conditions was shown in Fig. 4, Fig. 5 and Fig. 6.

It can be seen from the figure that under normal maximum drilling conditions, the stress of the mandrel is greater at the two grooves near the lower end; the first groove is the thread-cutting groove, and the second groove is the end groove. Among them, the maximum stress of the mandrel is 447.9 MPa, which

occurs at the thread retracting groove near the root of the mandrel thread, and the transverse groove is 445.1 MPa.

In addition, there are many cross-section changes in the upper part of the mandrel inside and outside the pipe, and there are several hydraulic channels and connecting holes in the pipe wall, so special attention needs to be paid to the groove. As shown in Fig. 6, the maximum stress at the connecting hole slot is 238.1MPa.

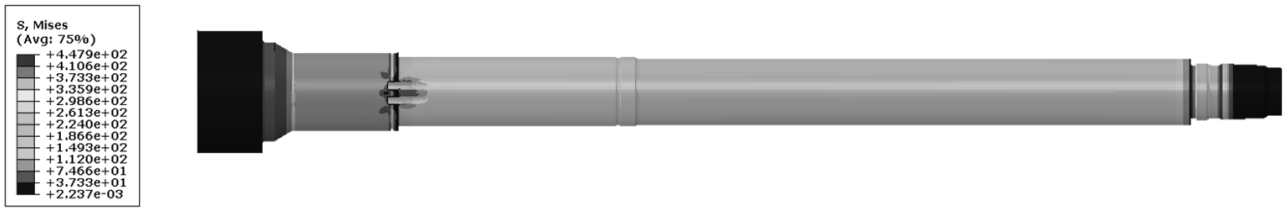

Fig. 4 *Overall stress cloud image of spindle*

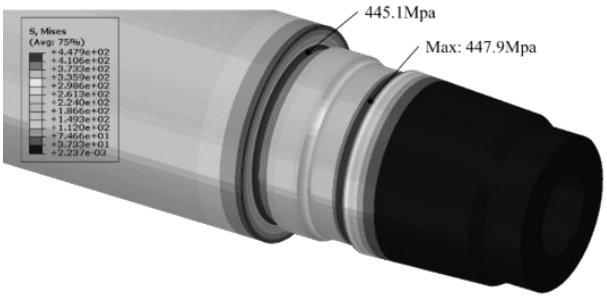

Fig. 5 *Stress cloud view of lower mandrel*

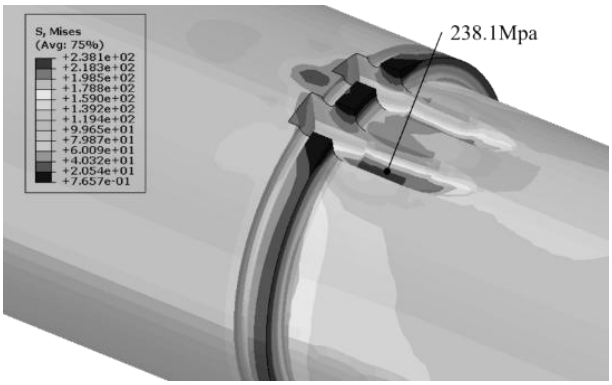

Fig. 6 *Local stress cloud image of the trench*

The spindle material is set to 15-15HS MAX alloy steel, σs=965MPa, and the safety factor of selected spindle design is 1.7~2.2.

In order to further study the mechanical properties of the rotating mandrel under different working conditions, the static characteristics of the rotating mandrel under multiple load conditions were calculated and the results were analyzed. It mainly includes "bit weight 100kN, 120kN, 140kN, 160kN, 180kN, 200kN, torque 9kN·m, 11kN·m, 13kN·m, 15kN·m, 17kN·m, 19kN·m".

3.2 Variable torque condition analysis

Firstly, the stress influence rule of torque on rotating mandrel under 140kN bit weight and 20kN push force is explored. The stress cloud diagram under variable torque condition is shown in Fig. 7.

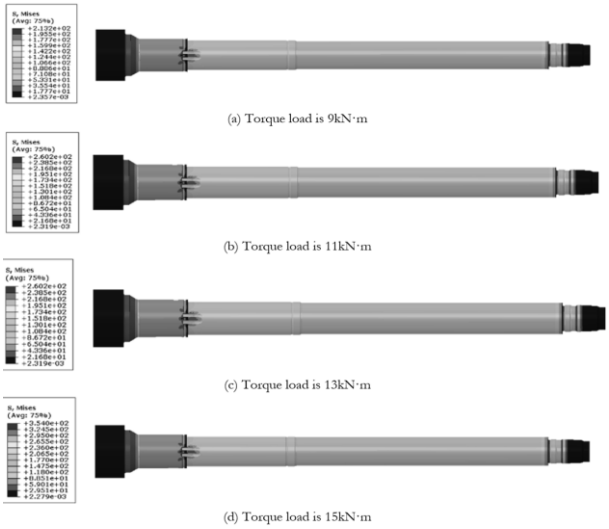

Fig. 7 *Force cloud diagram of torque load variation*

The curve of the maximum Mises stress on the rotating mandrel with the torsion load is shown in Fig. 8. With the increase of the torque, the maximum stress at the retracting slot at the thread root increased, obviously there was a phenomenon of stress concentration. As another weak point on the rotating mandrel, the maximum stress at the upper groove changes with the torque curve as shown in Fig. 9. As the torque increases from 9kN·m to 19kN·m, the maximum stress at the groove increases from 213.2Mpa to 447.9Mpa; However, the stress increase amplitude at the groove is smaller than that at the thread root.

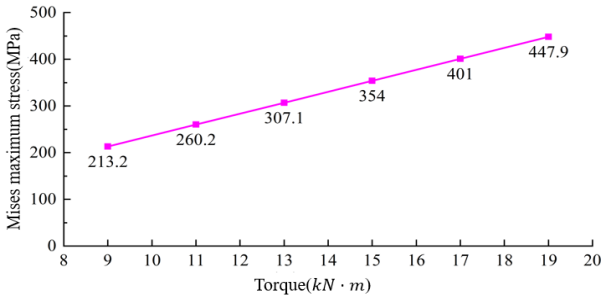

Fig. 8 *Curve of the maximum stress at the retracting groove at the root of thread with torque*

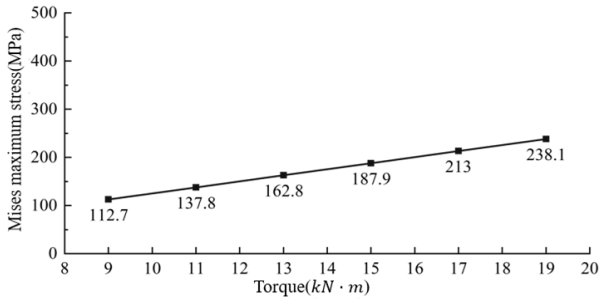

Fig. 9 *Curve of maximum stress at groove with torque*

3.3 Analysis of variable weight on bit

Subsequently, the law of influence of weight on bit on the stress of rotating mandrel under 19kN·m torque and 20kN push force is explored. The stress cloud diagram under each weight on bit load is shown in Fig. 10.

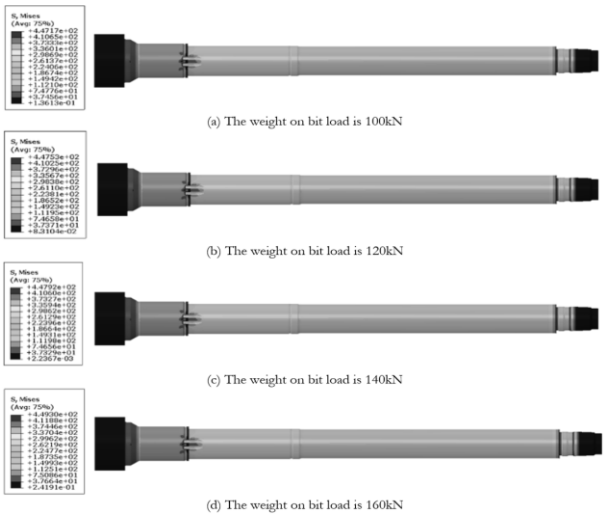

Fig. 10 *Force cloud diagram of weight on bit load variation*

As shown in Fig. 10, the maximum Mises stress on the rotating mandrel increased with the increase of weight on bit from 100kN to 200kN at 20kN push force and 19kN·m torque, but the change was minor.

For further reference to Fig. 11 and Fig. 12, with the increase of weight on bit, the stress changes in the groove and groove at the root of the thread are relatively small, far less than the impact of torque changes on the stress of the mandrel.

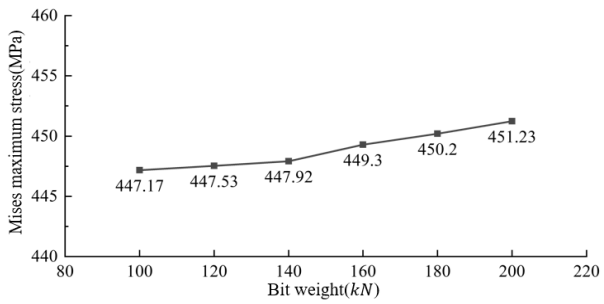

Fig. 11 *Curve of the maximum stress at theretracting groove at the root of thread with torque*

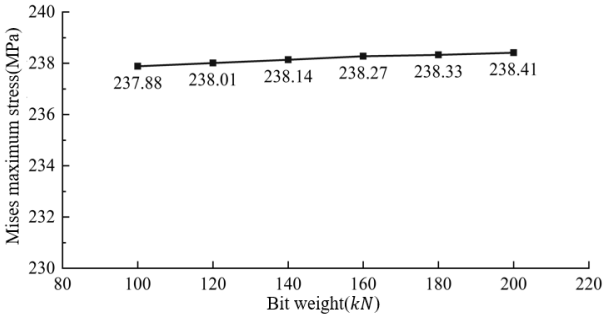

Fig. 12 *Curve of maximum stress at groove with torque*

3.4 Analysis of stuck drilling conditions

If the mandrel is lifted with a force of 1000kN in the case of stuck drilling, the stress cloud diagram is shown in Fig. 13. Under the extreme working condition of stuck drilling, the stress of the mandrel is greater at the tool release groove near the thread root, but the maximum stress value occurs at the groove of 236.7Mpa.

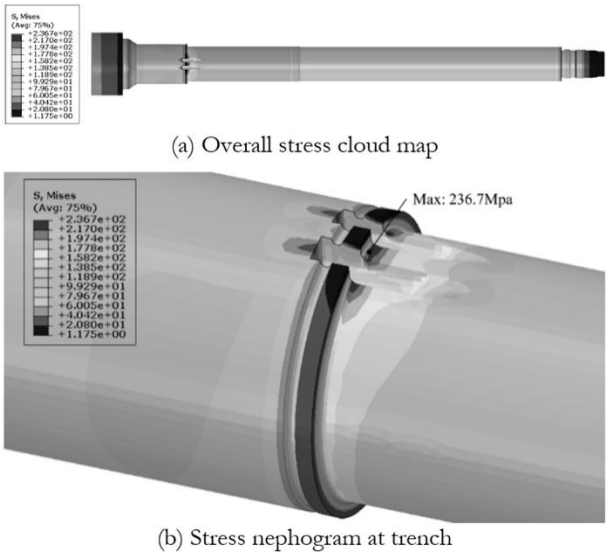

Fig. 13 *Stress nephogram at trench*

4 Life calculation

Fe-safe is a finite element model-based fatigue life analysis software developed by Safe Technology [12]. The Fe-safe software provides the user with a very complete material library, and the user can modify the material model according to the actual needs, and the load spectrum definition method in the software is flexible to support the calculation of the fatigue life of the structure under various loading modes. The software comes with a variety of fatigue life algorithms, such as fatigue algorithm based on maximum stress/strain, fatigue algorithm based on Von-Mises equivalent stress/strain, and Brown-Miller fatigue algorithm [13] based on critical surface. The fatigue analysis process for rotating mandrel is shown in Fig. 14. The fatigue analysis of Fe-safe needs to be based on the results of other finite element calculation software,

so the rotating mandrel has previously been modeled using Abaqus software and output the required stress/strain parameters.

After reading the stress variables at the nodes of the finite element model, Fe-safe processes the data according to the chosen algorithm. For example, for Brown-Miller analysis based on the critical plane, the software calculates the time history of shear strain, normal strain, shear stress, and normal stress on the three possible critical planes. The fatigue damage on each plane is calculated separately by Palmgren-Miner's rule [14]. The Rainflow algorithm [15] is used to count the number of fatigue cycles on each node, and the fatigue life of the structure is obtained.

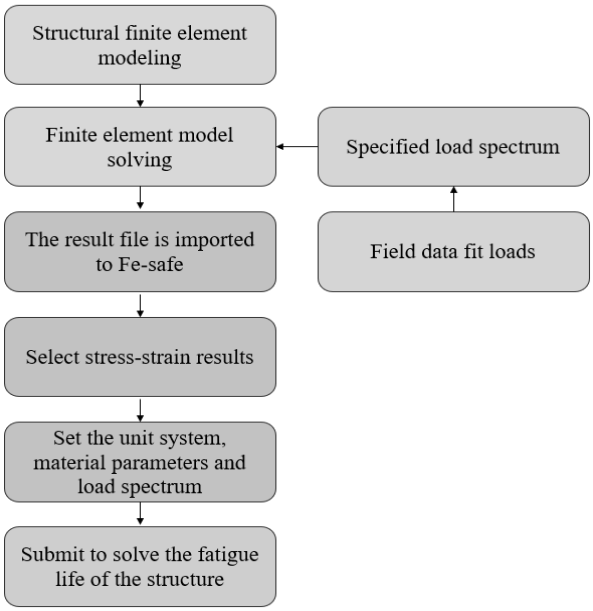

Fig. 14 *Flow chart of fatigue life analysis*

Based on the fatigue life prediction algorithm [16] (Principal stress), the fatigue damage model is shown in equation (12). The algorithm decomposed the stress into a series of planes, which were cross-swept in increments of 10°. Fatigue cycles were obtained on each plane, and the fatigue life was calculated using Goodman mean stress correction [17].

$$u(x,t)=\sum_{i=1}^{2} N_i(x)u_i(t) \tag{12}$$

Where:

$u(x,t)$…The stress time history at position x inside the element,

$N_i(x)$…The finite element shape function of node i at location x,

$u_i(t)$…The nodal stress time history of node i.

In order to verify the accurate value of the S-N curve in Fe-safe, the S-N fatigue curve of 15-15HS MAX alloy steel is fitted with the ncodeDL module in ANSYS. The results are shown in Fig. 15 below, and the results are basically consistent with Fe-safe in high-cycle fatigue section.

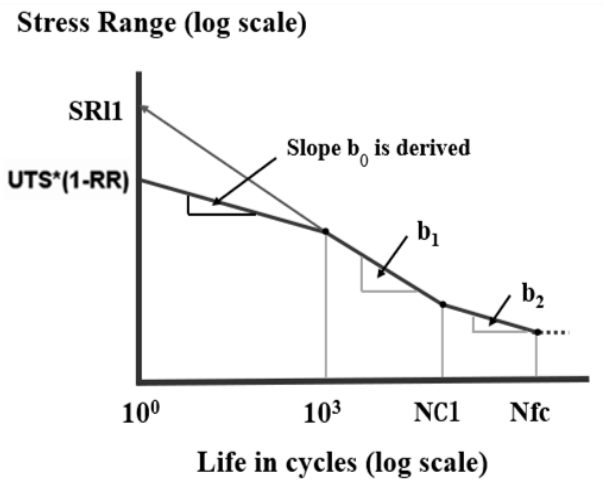

Fig. 15 *NcodeDL fits the S-N curve*

The load on the top of the bit was fitted to the sinusoidal load curve as shown in Fig. 16 according to relevant literature and field data while drilling. The spindle speed could reach 180rpm (3r/s) and the frequency of the load spectrum was set to 3.

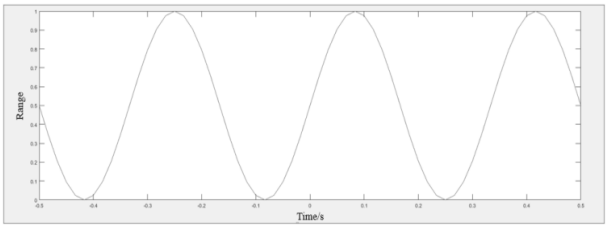

Fig. 16 *Sinusoidal load curve*

The life of the model was predicted by Morrow Brown-Miller model, and the predicted life results were shown in the fatigue life cloud diagram in Fig. 17. The fatigue life of the rotating mandrel model was 106.32s under continuous working conditions of weight on bit of 140kN, torque of 19kN·m, push force of 20kN and 180rpm. About 580.36h.

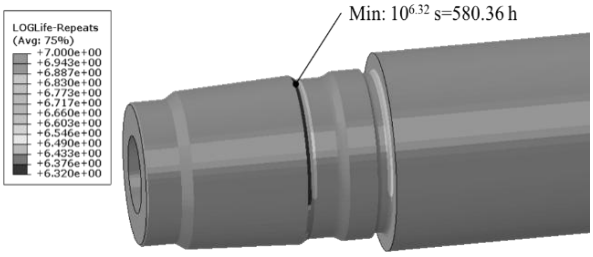

Fig. 17 *Cloud image of fatigue life under maximum working conditions*

If the torque is reduced from 19kN·m to 17kN·m; As shown in Fig. 18, the rotating mandrel model has a fatigue life of 106.851s (about 1971.05h) under continuous working conditions of weight on bit of 140kN, torque of 17kN·m, push force of 20kN and 180rpm, and the life of the mandrel is extended.

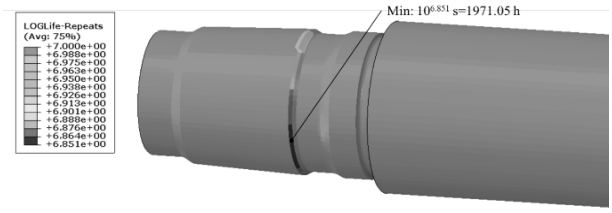

Fig. 18 *Cloud image of fatigue life after torque reduction*

According to the analysis of field data, the working time of 580.36h is relatively conservative, and the corrected working time of 309.083h under continuous working conditions with a weight on the bit of 140kN, torque of 19kN·m, push force of 20kN and 180rpm can be obtained by further modifying the load spectrum. The following table further displays the obtained life matrix.

The life mandrel matrix represents the service life of the main mandrel under the dual factors of screw speed and torque. For details, see Fig. 19. The way the life matrix is spread out matches the features of the S-N curve, showing that the lifespan in the low-load area is much longer than in the heavy-load area, which aligns with the lifespan traits of the main spindle under high-cycle fatigue [18]. According to the revised 180rpm, the life of the limit working condition at 19kN·m is 309.083h. In the case of torque conditions below 11kN·m, the main spindle can be considered as having an infinite life without considering the downhole vibration shock load [19].

Tab. 2 *Life matrix*

Life span h		Mandrel torque (Top drive torque-No-load torque) kN·m				
		12	13	14	15	16
Spindle speed (Screwspeed +Top drive speed) rpm	110	93281.35	36652.425	15450.107	6964.891	3354.148
	120	86026.131	33598.056	14162.598	6384.483	3074.636
	130	79408.741	31013.591	13073.168	5893.369	2838.126
	140	73736.683	28798.335	12139.369	5472.414	2635.402
	150	68820.908	26878.445	11330.078	5107.586	2459.709
	160	64519.6	25198.541	10621.948	4788.362	2305.977
	170	60724.329	23716.275	9997.128	4506.694	2170.331
	180	57350.754	22398.704	9441.732	4256.322	2049.757
	190	54332.295	21219.825	8944.798	4032.305	1941.875
	200	51615.679	20158.833	8497.558	3830.690	1844.781

Life span h		Mandrel torque (Top drive torque-No-load torque) kN·m				
		17	18	19	20	21
Spindle speed (Screwspeed +Top drive speed) rpm	110	1700.701	906.585	505.773	294.057	178.323
	120	1558.976	831.036	463.625	269.552	163.463
	130	1439.054	767.110	427.962	248.817	150.889
	140	1336.265	712.316	397.393	231.045	140.111
	150	1247.180	664.829	370.900	215.642	130.770
	160	1169.232	623.277	347.719	202.164	122.597
	170	1100.453	586.613	327.265	190.272	115.385
	180	1039.317	554.024	309.083	179.701	108.975
	190	984.616	524.865	292.816	170.243	103.239
	200	935.385	498.621	278.175	161.731	98.077

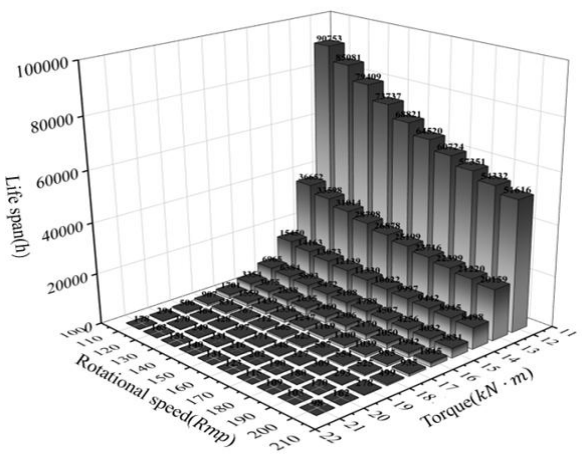

Fig. 19 *Life distribution*

5 Fitting formula and algorithm setting

5.1 Power function fitting

In the case of a single variable, both life-mandrel speed and life-mandrel torque can be fitted as power functions, and the influence of torque on life is greater than that of speed.

According to the life-load characteristics, the life at single speed can be synthesized into a power function. Two kinds of power function formulas are fitted as follows, a power function with correction term, and an ordinary power function [20]. It is verified that the two power functions fit the actual calculation situation, and the power function curve without correction term is more conservative under heavy load.

Tab. 3 *Life time curve with torque at different spindle speeds*

Spindle speed/rpm	Amend	Conserved
110	T=3.787×10^17×x^-11.68+79.78	T=3.482×10^17×x^-11.65
120	T=4.068×10^17×x^-11.75+92.85	T=3.656×10^17×x^-11.7
130	T=3.755×10^17×x^-11.75+85.71	T=3.656×10^17×x^-11.7
140	T=3.487×10^17×x^-11.75+79.59	T=3.134×10^17×x^-11.7
150	T=3.254×10^17×x^-11.75+74.28	T=2.925×10^17×x^-11.7
160	T=3.051×10^17×x^-11.75+69.64	T=2.742×10^17×x^-11.7
170	T=2.872×10^17×x^-11.75+65.54	T=2.581×10^17×x^-11.7
180	T=2.712×10^17×x^-11.75+61.9	T=2.437×10^17×x^-11.7
190	T=2.569×10^17×x^-11.75+58.64	T=2.309×10^17×x^-11.7
200	T=2.441×10^17×x^-11.75+55.71	T=2.193×10^17×x^-11.7

5.2 Fatigue cumulative damage law

According to the linear Miner fatigue rule in the fatigue cumulative damage law, the fatigue damage in the whole working cycle can be linearly added.

$$D = \sum_{i=1}^{k} D_i = \sum_{i=1}^{k} \frac{n_i}{N_i} \tag{13}$$

The damage of the component subjected to n_i sub-cycles under the action of stress range is $D_i = n_i / N_i$, then the total damage of each component subjected to n_i sub-cycles under the action of k stress ranges can be defined as D, and the failure criterion D=1. Therefore, the fatigue accumulation can be converted into the fatigue time accumulation. When the following formula is satisfied, the component is destroyed [21].

$$\sum_{i=1}^{k} \frac{T_i'}{T_i} = 1 \tag{14}$$

Where:

k…The total number of working conditions experienced,

T_i' …A single working time,

T_i …The life cycle under working conditions. It can be calculated by selecting the corresponding life fitting curve of the screw speed and defined T_i' / T_i as the fatigue damage coefficient Δ_i. When the cumulative fatigue damage coefficient is 1, it can be regarded as a crack in the stress concentration position of the main spindle and the member reaches the life limit.

6 Conclusion

The finite element static simulation calculation and stress and life analysis were carried out on the mandrel of push-type rotary steering tool under different combination conditions of torque and different bit load. The main conclusions are as follows:

- (1) Under the maximum working conditions of weight on bit 140kN, push force 20kN and torque 19kN·m, the maximum equivalent stress on the rotating mandrel is 447.9MPa, and the maximum equivalent stress is located at the cutting groove at the root of the thread. The safety factor of the mandrel is 2.15, which meets the strength safety requirements of the corresponding material. The equivalent stress on the spindle as a whole increase with an increase in torque. When the push force is 20kN, the maximum equivalent stress changes little with the increase of bit weight. When the torque is compared with the weight on the bit under the maximum working condition, the influence of torque on the strength is more than 98%.
- (2) The corrected life of the rotating mandrel under the maximum working condition is about 309.083 hours. When the life limit is reached, cracks may occur at the root of the thread, leading to the fracture of the mandrel. Reducing the torque and speed within the range of meeting the drilling requirements helps to improve the overall life of the mandrel.
- (3) Both life-mandrel speed and life-mandrel torque can be fitted as power functions, and the influence of torque on life is greater than that of speed. The life distribution from the life matrix matches the S-N curve, showing that the lifespan under low load is much longer than under heavy load, which aligns with the high-cycle fatigue traits of the main spindle.

References

[1] ZHANG, Q.S. (2021). New progress and development direction of modern guided drilling technology. *Chinese science and technology journal database industry A*, No. 2, pp. 58.

[2] ZHENG, D.S., GAO, D.L., FENG, J.P., ZHANG, H.B. (2011). Study on deflection performance of backup and directional types of rotary steering tools. *Oil Drilling & Production Technology*, Vol. 33, No. 6, pp. 10-13. DOI: 10.13639/j.odpt.2011.06.005

[3] LI, J., LI, D.C., ZHANG, H., WANG, H. (2019). The influencing factors of the inclination ability of push-the-bit rotary guiding tool. *Oil Drilling and Production Technology*, Vol. 41, No. 4, pp. 460-466. DOI: 10.13639/j.odpt.2019.04.010

[4] BI, Y.T., LIU, G.H., MA, Q.M., YANG, N.N., ZHU, J.R., LIU, J.X. (2021). Analysis of Statics Characteristics of Static Push-the-Bit Rotary Steerable System. *China Petroleum Machinery*, Vol. 49, No. 7, pp. 1-7. DOI: 10.16082/j.cnki.issn.1001-4578.2021.07.001

[5] ZENG, B., ZHENG, Y., WU, P., ZHOU, F., HUANG, M., BAI, Y., XIA, C. (2022). Simulation Analysis of Combined Mechanics of the Thrust Rotary Guide Drill. *Scientific Programming*, Vol. 2022, No. 1, pp. 4639555. https://doi.org/10.1155/2022/4639555

[6] JIA, J.B., LAN, H.B., JIAN, Z.J., SUN, S.X., MENG, W. (2023). Bending stress distribution rules of the 475 static push-the-bit Rotary Steerable Bottom-Hole Assembly (RSBHA). *Chinese Journal of Geophysics*, Vol. 66, No. 1, pp. 95-100.

[7] HE, J.J., MAO, L.J., YANG, S., QIN, C.H., ZHAO, Q.Y., WEI, X.G. (2024). Mechanical Property Analysis of Bottomhole Assembly with Decentralized Rotary Steering System. *China Petroleum Machinery*, Vol. 52, No. 4, pp. 41-48. DOI: 10.16082/j.cnki.issn.1001-4578.2024.04.006

[8] ZHANG, G.W., HOU, P.P., LI, J.Q., MA, J.Q. (2021). Study on vibration characteristics of guiding shaft of new directional rotary steering drilling tool. *Coal Science and Technology*, Vol. 49, No. 10, pp. 177-184. DOI: 10.13199/j.cnki.cst.2021.10.024

[9] LIU, Y.Z., CHEN, L.Q., CHEN, W.L. (2019). *Vibration Mechanics* [M]. Beijing: Higher Education Press.

[10] HOU, P.P. (2021). Research on Guiding Principle and Dynamic Characteristics of Fully Rotating Closed-loop directional steering drill [D]. Xi'an Shiyou University.

[11] WANG, S.Y. (2015). Design of Shell of Rectangular Pipe Jacking Machine Based on Solid-Works Modeling. *Tunnel Construction*, Vol. 35, No. 3, pp. 274-278.

[12] HAO, H.S., LIU, Y., LIU, D., XING, Y., JIAO, J.F. (2021). Fatigue Life analysis of high-strength bolt for end-plate Connection based on refined finite element. *China Science paper*, Vol. 16, No. 8, pp. 818-824+848.

[13] DARBAN, H., NOSRATI, M., & DJAVANROODI, F.(2015). Multiaxial fatigue analysis of stranded-wire helical springs. *International Journal of Damage Mechanics*, Vol. 24, No. 7, pp. 1013-1025.

[14] CHEN, N. Z., WANG, G., & SOARES, C. G. (2011). Palmgren-Miner's rule and fracture mechanics-based inspection planning. *Engineering Fracture Mechanics*, Vol. 78, No. 18, pp. 3166-3182. https://doi.org/10.1016/j.engfracmech.2011.08.002

[15] PERPINA, X., JORDA, X., VELLVEHI, M., REBOLLO, J., & MERMET-GUYENNET, M. (2011). Long-Term Reliability of Railway Power Inverters Cooled by HeatPipe- Based Systems. *IEEE Transactions on industrial Electronics*, Vol. 58, No. 7, pp. 2662-2672. DOI: 10.1109/TIE.2010.2087298

[16] ZU, H.Y., GENG, C.L., LI, D.Q., SONG, Y.J. (2018). Research on fatigue performance test and life prediction for stator rubber of PCP. *Journal of Mechanical Strength*, Vol. 40, No. 1, pp. 195-199. DOI: 10.16579/j.issn.1001.9669.2018.01.033

[17] CHEN, M., SHAO, F., YU, H.T., BAI, L.Y. (2020). Research on Fatigue Life Prediction Model of Local Stress Strain Method based on Average Stress. *Equipment Manufacturing Technology*, No. 7, pp. 57-60+86.

[18] ABD-ELTWAB, A.A., ELSYED AYOUB, W., EL-SHEIKH, M.N., SAIED, E.K., GHAZALY, N.M., GOMAA, A.A. (2024). An Investigation into Forming of Gears Using Rotary Forging Process. *Manufacturing Technology*, Vol. 24, No. 4, pp. 539-551. DOI: 10.21062/mft.2024.068

[19] WANG, Z., YIN, H. (2025). Titanium Alloy Turning Machining Model and Quality Analysis Based on Finite Element Analysis. *Manufacturing*

Technology, Vol. 25, No. 3, pp. 413-423. DOI: 10.21062/mft.2025.036

[20] UHRÍČIK, M., PALČEK, P., CHALUPOVÁ, M., KUCHARIKOVÁ, L., PASTIEROVIČOVÁ, L., MEDVECKÁ, D., ET AL. (2023). Structural and Fractographic Analysis of Aluminum Alloy before and after Fatigue Loading. *Manufacturing Technology*, Vol. 23, No. 5, pp. 725-731. DOI: 10.21062/mft.2023.067

[21] SHI, P.J., HU, M.Y., DING, Y.J., ZHANG, G.X., YU, J.W., ZHANG, P.W. (2020). Fatigue life of 2.5D carbon fiber reinforced silicon Carbide matrix composites(in Chinese). *Scientific and Technological Innovation*, No. 19, pp. 1-4.